Available online at www.sciencedirect.com
ScienceDirect
Comput. Methods Appl. Mech. Engrg. 357 (2019) 112587
Computer methods in applied mechanics and engineering
www.elsevier.com/locate/cma

MAP123: A data-driven approach to use 1D data for 3D nonlinear elastic materials modeling

Shan Tang[a,c], Gang Zhang[b], Hang Yang[a], Ying Li[d,*], Wing Kam Liu[e,*], Xu Guo[a,c,**]

[a] State Key Laboratory of Structural Analysis for Industrial Equipment, Department of Engineering Mechanics, Dalian University of Technology, Dalian, 116023, PR China

[b] School of Mechanical and Electrical Engineering, Wuhan Institute of Technology, Wuhan, 430200, PR China

[c] International Research Center for Computational Mechanics, Dalian University of Technology, PR China

[d] Department of Mechanical Engineering and Institute of Materials Science, University of Connecticut, Storrs, CT 06269, USA

[e] Department of Mechanical Engineering, Northwestern University, 60208, USA

Received 11 April 2019; received in revised form 8 July 2019; accepted 7 August 2019
Available online 19 August 2019

Highlights

- MAP123 can decompress 1D data into 3D to solve BVP problem without material laws.
- MAP123 is implemented and employed to solve BVP problems by 1D data.
- MAP123 demonstrates a way to express 3D material law through two sets of 1D experimental data.
- MAP123 can analyze the mechanical response under finite deformation.

Abstract

Solving three-dimensional boundary-value engineering problems numerically requires material laws. However, it is difficult to build the material laws in three dimension, since the material behaviors are usually measured by one-dimensional uniaxial tension/compression experiments. In this way, the material behavior in the three-dimension is 'compressed' into one-dimensional data. Here we propose a new method, coined MAP123 (map data from one-dimension to three-dimension), to decompress the one-dimensional data into three dimension for nonlinear elastic material modeling without the construction of analytic mathematical function for the material law. The decomposition of stress and strain into deviatoric and spherical parts for isotropic nonlinear elastic materials at finite deformation makes this data-driven approach work quite well. Several examples are used to demonstrate the capability of MAP123, such as a rectangular plate with a circular hole under uniaxial tension. Corresponding experiments are also carried out to further verify the MAP123 method. Based on the proposed approach, uniaxial experiment is suggested to measure the deformation in three directions not only the force and extension along the loading direction. Limitation of the proposed MAP123 approach is also discussed.

Keywords: Data-driven approach; Material law; Compressed data; Finite element analysis

* Corresponding authors.
** Correspondence to: Department of Engineering Mechanics, Dalian University of Technology, Dalian, 116023, PR China.
E-mail addresses: yingli@engr.uconn.edu (Y. Li), w-liu@northwestern.edu (W.K. Liu), guoxu@dlut.edu.cn (X. Guo).

https://doi.org/10.1016/j.cma.2019.112587

1. Introduction

The boundary-value problem plays a unique and critical role in mechanics and physics [1,2]. Many problems involved in engineering applications have to be transformed into boundary-value problems. Then numerical methods such as finite element analysis (FEA) are used to find the solutions of these boundary-value problems [3,4], aiding the engineers to design and optimize the body and structure involved. A set of equations for boundary-value problem usually is combined with two types of equations: conservation laws and material/constitutive laws [5–10]. The conservation laws usually are derived from the universal physical principles while the constitutive laws are formulated based on the physical understanding and experimental observations of materials [2,11].

It is not easy to build an accurate material model covering arbitrary stress-states, depending strongly on the mathematical technique and the intuition on material behaviors. Some basic requirements on the material model should also be satisfied such as objectivity. Even for nonlinear elastic materials at finite deformation, the neo-Hookean model, Odgen model and Arruda–Boyce model are widely used now though it is built through a long-time efforts [12–14]. For all these models, analytic mathematical function of energy density must be proposed first. Then the stress–strain relationship is derived through the analytic function. Nevertheless, it is shown that neo-Hookean model, Arruda–Boyce model and Odgen model may not capture the material accurately under compression and/or tension for new materials, such as, silicone rubber fabricated in our experiments [15], see Fig. 1. In comparison with experiments under compression, these three models work well at the small deformation regime but not very accurate when the deformation is large enough. In comparison with experiments under tension, the neo-Hookean model is the worst. The Odgen and Arruda–Boyce models also show some discrepancies compared with experimental data even when the imposed strain is larger than 10%. Therefore, data-driven material models should be developed to circumvent the traditional way for material models with analytic mathematical form [16–21]. For instance, Ortiz and co-workers [5,7,8] proposed a new computational paradigm to bypass building material models. There is no material model assumed *a priori* but purely using experimental data to drive the computation to solve boundary-value problems based on the optimization in the phase space of stress and strain. This data-driven approach can ignore the inner mechanism of material laws, lessen the difficulty to choose the existing nonlinear elastic models and calibrate the related parameters (often more than 2) involved. These existing material models also may not be good enough for many new emerging materials because these existing models only can consider the well-known mechanisms of existing materials. The data-driven approach can accelerate the process for the engineering design [22–26]. Recently, it is further developed for real-time topology optimization [27].

Until now, because the uniaxial tension/compression on the specimen of materials is the most convenient way for physical measurements, it is relatively easy to obtain experimental data in the one-dimension. However, the generalization of experimental data from one-dimension (1D) to describe its behavior in three-dimension (3D) body under arbitrary loading is not straightforward. The 1D data is in analogy to the compressed data in data science, illustrated as follows. Many sampling data-sets are in the high dimensional space, as presented in Fig. 2a. Principal Component Analysis (PCA) is a technique which is widely used for applications such as dimensionality reduction, lossy data compression, feature extraction and data visualization [28–31]. Due to PCA transformation, the decompressed data cannot be exactly the same as the original data. This compression and decompression of data-sets can be demonstrated by an application to a binary image shown in Fig. 2b, expressed in the digits of 0 and 1. PCA is an analogy to choose the most 0 or 1 for each pixel (an element in the matrix). Applying PCA, the data-sets (x) for the images can be compressed in a form with small size (x_c) for the convenience of data storage and transferring. The compressed image can be decompressed through inverse PCA ($\widetilde{x}$). The recovered image cannot be exactly the same as the original one. The elements which are different from the original images are marked by dashed red boxes shown in Fig. 2b. We are facing the similar situation in mechanics but there are still some differences. A series of data such as digits of images or voice are easy to be obtained. However, the material data under arbitrary stress-state is not easy to be obtained through experiments. The mostly available experimental data is in the 1D. Here the term 'compressed' is defined by us in mechanics means that the material behaviors at any stress-states are compressed and reserved in 1D data. The 1D compressed data is expected to be extracted for 3D computation.

The approach initiated by the prominent mechanician such as Hill [32] developing plasticity theory in 1950s inspires us to find a new way. This method, called MAP123 (map data from one-dimension to three-dimension), is proposed to decompress the measured 1D data for 3D computation in the present work. The MAP123 method can be employed to solve the 3D boundary-value problems, purely driven by the 1D compressed data without

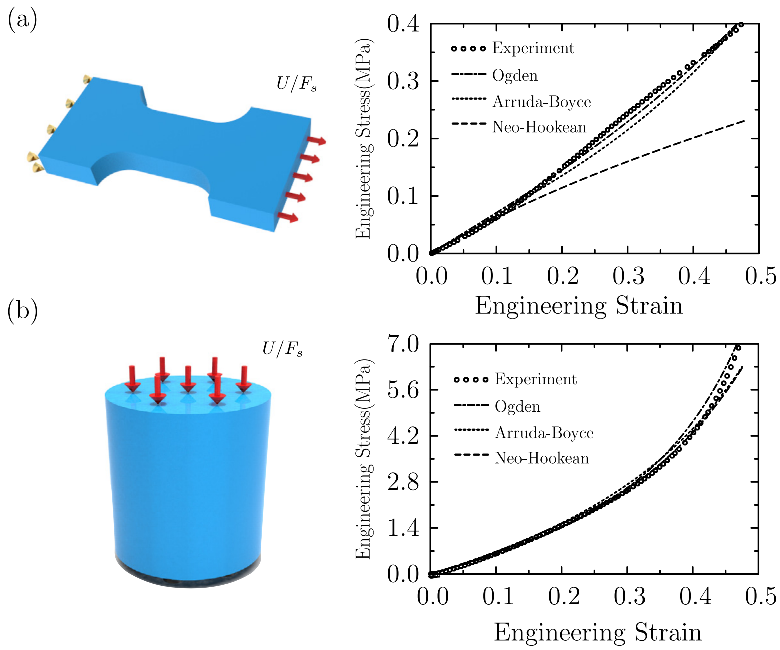

Fig. 1. Experimental measured stress–strain data for fabricated silicone rubber in our experiments under (a) tension and (b) compression respectively. The neo-Hookean model, Arruda–Boyce model or Odgen model are used to model the experimentally measured data. The neo-Hookean model, Arruda–Boyce model or Odgen model cannot perfectly fit the experimental data when the deformation is large.

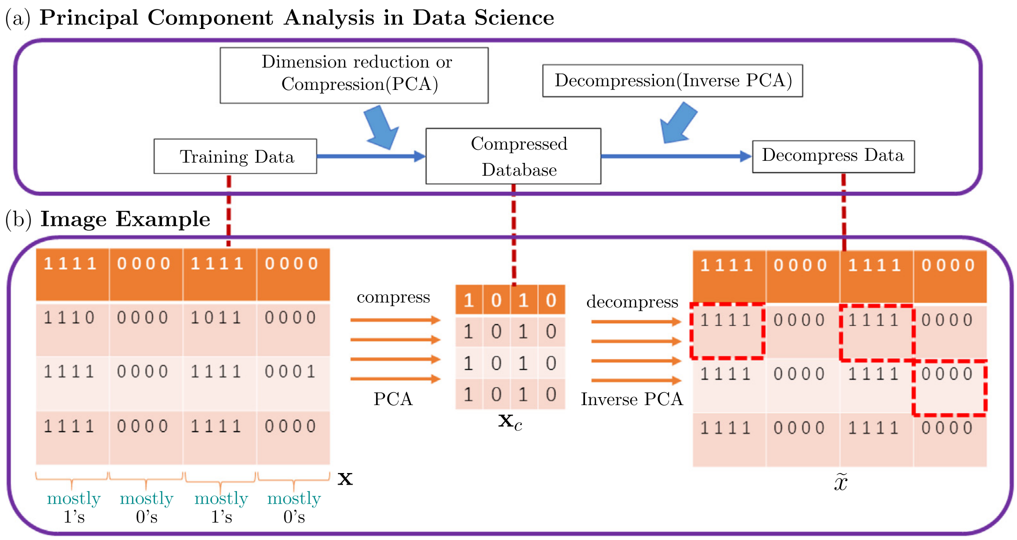

Fig. 2. (a) Principal component analysis (PCA) in data science. Many original sampling data sets are in the high dimensional space. The PCA can be used to reduce the high dimension of data into lower dimension, so-called 'compressing the data'. The compressed data can be decompressed for future applications. (b) PCA on a binary image. The original image can be compressed into the image in the middle through PCA, choosing the most 0 or 1 for each pixel (an element in the matrix). The compressed image can be decompressed but some pixels are not the same as the original ones. This figure is adapted from the research report of Prof. Wing Kam Liu's group at Northwestern University.

constructing the analytic mathematical function for material laws. In Section 2, we will discuss the decomposition of the second PK stress and Green strain into the deviatoric and spherical parts in the MAP123 method and the implementation of the proposed method through finite element method. In Section 3, the proposed MAP123 method will be applied to simulate 3D boundary-value problems under different loading conditions, in comparison with direct numerical simulation with the reference material model. The proposed MAP123 is also verified by

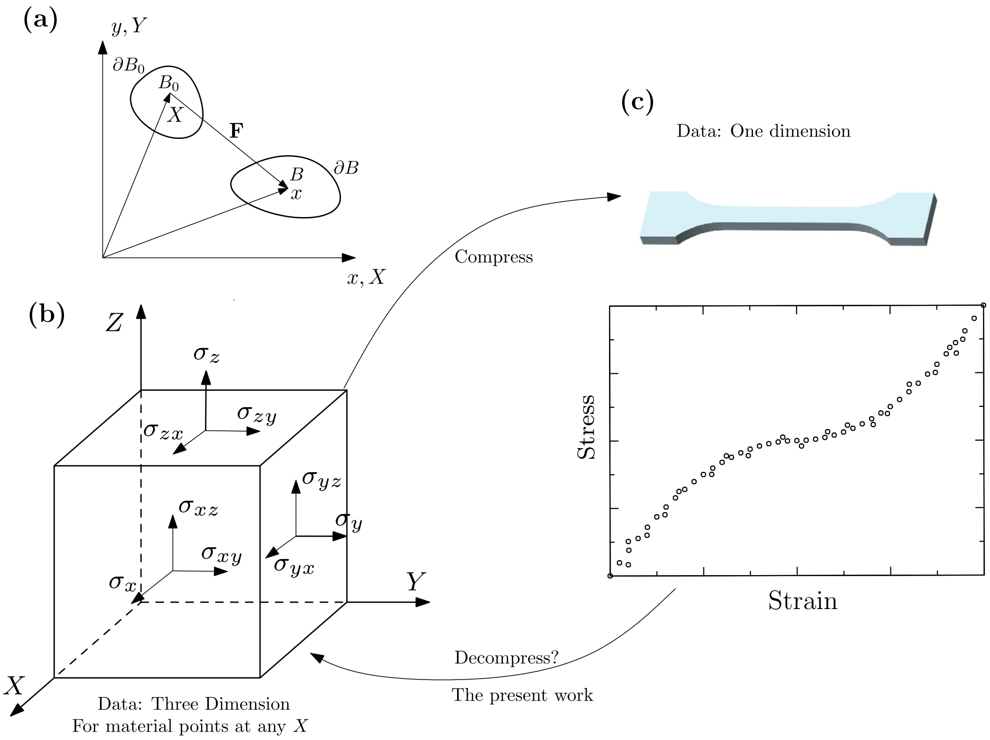

Fig. 3. (a) A material point at point X moves to the current point of x during the deformation. (b) The stress and strain at the material point X are in a three-dimensional state. (c) Unzipping compressed one-dimensional data to drive the three dimension computation.

experiments on the silicone rubber. All these results prove the proposed method can solve these problems. This approach shows the advantage that the experimental data obtained under uniaxial tension/compression condition can be used to solve boundary-value problem directly. Few conclusion remarks are given in Section 4.

2. Decompression of 1D data into 3D

2.1. Data expansion from 1D to 3D in MAP123

We will briefly give the key theoretical aspects of MAP123. The detailed MAP123 concept is given in Appendix A. The main idea can be illustrated in Fig. 3. For a material point at X in the continuum body, it moves to the point of x in the current configuration. The stress and strain at the material point X of the continuum body should be in a 3D state. However, only 1D stress–strain data is easy to be obtained by numerical/physical experiments under uniaxial tension/compression. This 1D data can be decompressed to drive the 3D computation in the boundary-value problems during finite element analysis. The right Cauchy–Green strain E_{ij} and second Piola–Kirchhoff (PK) stress S_{ij} are adopted as the strain and stress measures in our theory. Here $i, j = 1, 2, 3$ for 3D analysis. It is assumed here that the material belongs to the family of isotropic nonlinear elastic solids, which can experience finite deformation.

The measured 1D data can be finally generalized to 3D to obtain the expression for second PK stress. The 3D stress can be written as:

$$S_{ij} = \sum_{I=1}^{3} \gamma E'_I \, (N_I)_i \, (N_I)_j + S_m \delta_{ij} \tag{1}$$

in which γ is given through the coaxial relationship between deviatoric stress and deviatoric strain:

$$\frac{S'_1}{E'_1} = \frac{S'_2}{E'_2} = \frac{S'_3}{E'_3} = \gamma \tag{2}$$

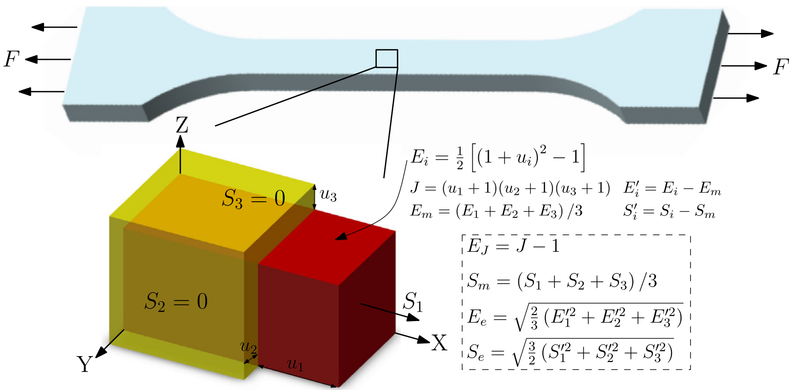

Fig. 4. The visualization of data generation by the experiments under uniaxial tension. (For interpretation of the references to color in this figure legend, the reader is referred to the web version of this article.)

The detailed derivation of this relationship and its condition for satisfaction are given in Appendix B. Here, S_I and S_I' are the principal stress and deviatoric principal stress, respectively; E_I and $\mathbf{N}_I$ $(I = 1\dots3)$ are the eigenvalues and eigenvectors of strain, respectively; $S_I' = S_I - S_m$, $E_I' = E_I - E_m$ with $E_m = (E_1 + E_2 + E_3)/3$ and $S_m = (S_1 + S_2 + S_3)/3$; δ_{ij} is Kronecker delta symbol. The parameter γ can be obtained based on searching the measured experimental data in phase space (E_e, S_e) and (E_m, S_m) (or (E_J, S_m)). E_e and S_e are defined similar to those at the small deformation regime, that is, $E_e = \sqrt{\frac{2}{3}\left(E_1'^2 + E_2'^2 + E_3'^2\right)}$ and $S_e = \sqrt{\frac{3}{2}\left(S_1'^2 + S_2'^2 + S_3'^2\right)}$. $E_J = J - 1$ and $J = \det(\mathbf{F})$ where $\mathbf{F}$ is the deformation gradient.

The 1D data set of (E_e, S_e) and (E_m, S_m) (or (E_J, S_m)) can be generated as the following. Suppose we have a specimen under uniaxial tension, shown in Fig. 4. For uniform deformation, only the region at the center of specimen can be taken out for analysis (the region can be assumed as $1 \times 1 \times 1$ cubic without losing generality). Yellow color represents the original configuration and red color represents the configuration at the time step $t_{l,l=1\cdots N_s}$ where l represents the time step number and N_s is the total number of time step. Under uniaxial tension, only the strain components E_1, E_2 and E_3 exist and can be computed based on the recorded deformation of the specimen (that is, the displacements u_1, u_2 and u_3 shown in Fig. 4). The equations to compute E_1, E_2 and E_3 with the measured displacements are also given. Because of the symmetry of the specimen in y and z direction, the computed strain in y and z directions are equal $E_2 = E_3$. During the tensile experiment, the reaction force F can also be recorded by the test machine. With the known section area A_0 of the specimen, the second PK stress S_1 can also be computed by $S_1 = F/A_0/(1+E_1)$. S_2 and S_3 are zeros. Then $S_m = \frac{1}{3}S_1$. S_1 can be stored in a one-dimensional array: $[S_1]^{l=1\cdots N_s}$. In the following, [ ] means the quantity is stored as an array. Similarly, the strain components E_1, E_2 and E_3 can be stored as $[E_1]^{l=1\cdots N_s}$, $[E_2]^{l=1\cdots N_s}$ and $[E_3]^{l=1\cdots N_s}$ respectively. Then E_e can also be computed and stored as $[E_e]^{l=1\cdots N_s}$ while $[S_e]^{l=1\cdots N_s}$. Similarly, E_J, E_m or S_m can be computed and stored as $[E_J]^{l=1\cdots N_s}$, $[E_m]^{l=1\cdots N_s}$ or $[S_m]^{l=1\cdots N_s}$ respectively.

For online FEM simulations, the arbitrary deformation E_{ij} at each material point and the corresponding E_e can be computed. Searching the array of $[E_e]^{l=1\cdots N_s}$ to match the computed E_e, the corresponding S_e in the array of $[S_e]^{l=1\cdots N_s}$ will be used to find γ through Eq. (18) and the deviatoric part of stress can be updated. The similar procedure can be used to update the hydrostatic stress. Searching the array of $[E_m]^{l=1\cdots N_s}$ or $[E_J]^{l=1\cdots N_s}$ to match the computed E_m of each material point can find the corresponding hydrostatic stress in the array of $[S_m]^{l=1\cdots N_s}$ in the online computation.

Remarks. I. Physically, γ reflects the instantaneous shear modulus. The instantaneous bulk modulus is implied in the ratio between E_m and S_m. In fact, the proposed MAP123 avoids the construction of analytic mathematical form of the elastic energy to describe its mechanical response.

II. Under the uniaxial tension or compression along the x direction, it is evident $S_{11} \neq 0$ and $S_{22} = S_{33} = 0$. Then $S_m = \frac{1}{3}S_{11}$. For the strain $E_{11} \neq E_{22} = E_{33} \neq 0$. The experiment with DIC facility can measure the strain in y and z directions. The only component E_{11} is not enough because both the instantaneous shear modulus and bulk modulus are required to describe the hydrostatic stress vs. E_m.

III. The present work is limited to the compressible material and the incompressible case will be discussed in our future work. The additional constraints imposed by incompressibility actually can help in mapping the data from 1D to 3D because the data-set of mean stress vs. mean strain is not needed. However, it will be shown in the following that the finite element analysis is carried out under the displacement driven framework. The extra constraint of displacement caused by incompressibility also needs to be incorporated. This will increase the difficulty for finite element implementation. This can be overcome by other approaches, which will be discussed in the future.

IV. For nonlinear isotropic elastic materials, the second PK stress shares the same principal axes with right Cauchy–Green strain. This does not exist for elastoplastic materials. However, by virtue of concept of trial stress and strain, it is possible to design an algorithm to map the one-dimensional data into three-dimension, which can be used to drive three-dimension computation for elastoplastic materials. It is challenging and further work should be carried out.

3. Numerical implementation of MAP123

We now discuss the numerical implementation of MAP123, which is carried out within the displacement-driven FEA framework. The variational forms for the equilibrium equation of three dimensional body can be formulated [4]. The algorithm for stress update is summarized in the Box I and $|_{X_g}$ denotes the quantities at a Gauss point X_g. In the Box I, F_{ij} are the components of deformation gradient $\mathbf{F}$, S_{ij} are components of the second PK stress $\mathbf{S}$. C^0 displacement approximation is assumed first based on the interpolation of displacement of node u_i^A through shape function $\bar{N}^A$. Residual force vector and tangent stiffness matrix can be calculated, referring to Belytschko et al. [4]. Note that the 1D stress–strain data is in a discrete form. It is difficult to obtain its analytical derivatives. It is better to compute tangent stiffness matrix numerically.

4. Results and discussion

The proposed MAP123 will be compared to the approaches with given material laws by solving the same 3D boundary-value problems. The above algorithm for the proposed MAP123 method is implemented as a three dimensional eight-node element. Although the numerical examples shown in the following part look like a 2D problem, they are solved in 3D settings.

4.1. Numerical experiments for data-generation

We first demonstrate the concept by carrying out the numerical experiments of tension to generate the 1D data, in which the Odgen model [13] is employed for the material behavior. The Odgen model shows great applicability to model the nonlinear elastic materials, especially soft tissues. The form of the Ogden strain energy potential is given as

$$W = \frac{2\mu}{\alpha^2}\left(\bar{\lambda}_1^\alpha + \bar{\lambda}_2^\alpha + \bar{\lambda}_3^\alpha - 3\right) + \frac{1}{D}\left(J-1\right)^2 \tag{3}$$

where α is a material constant. One element with a unit length under uniaxial tension (the region with $1 \times 1 \times 1$ size shown in Fig. 4) is designed to generate the 1D data set $([E_e], [S_e])$ and $([E_J], [S_m])$ [33–36], referring to Fig. 4. Two sets of data (named M_A and M_B) are generated in the present work, as shown in Fig. 5a respectively. M_A and M_B are generated by Odgen model with parameters ($\mu = 0.3864$, $D = 2.4$ and $\alpha = 4.5$) and ($\mu = 0.3864$, $D = 2.4$ and $\alpha = 2$), respectively. M_A and M_B are used to drive 3D FEA computations according to the proposed MAP123 method without using any other material laws.

4.2. Physical experiments for data-generation

To verify the proposed MAP123, we also carry out the physical experiments to generate the 1D data. A silicone rubber is first synthesized and a specimen for the uniaxial tension is made through 3D printing. The obtained specimen is shown in Fig. 5b. The size of the specimen is also marked. Then the uniaxial tension on the specimen is performed by a universal testing machine SHIMADZU EZ-LX. We use DIC (Digital Images Correlation) testing facility to record the displacement of the specimen at each loading step. With the procedure discussed in Section 2, a set of data is generated, which is shown in Fig. 5b. This set of data will be used to drive 3D computations to simulate the voided specimen with the same silicone rubber according to the proposed MAP123 method. It will be discussed in the next section.

I. Compute the deformation gradient and its determinant

$$F_{ij}\big|_{X_g} = \delta_{ij} + \frac{\partial \bar{N}^A}{\partial X_j}\bigg|_{X_g} u_i^A$$

$$J = \det(F_{ij}\big|_{X_g})$$

II. Compute right Cauchy–Green tensor

$$C_{ij}\big|_{X_g} = \sum_{k=1}^{N} F_{ki}\big|_{X_g} F_{kj}\big|_{X_g}$$

III. Compute eigenvalues and eigenvectors of $C_{ij}\big|_{X_g}$ using Jacobian method

$$C_{ij}\big|_{X_g} \Rightarrow \begin{cases} a_{I=1\ldots3} \\ v_{I=1\ldots3} \end{cases}$$

where $a_{1\ldots3}$ are eigenvalues and $v_{1\ldots3}$ are the corresponding eigenvectors.

IV. Set the eigenvalues and eigenvectors of Green strain E and compute the effective strain E_e and the hydrostatic strain E_m

$$E_I = \frac{1}{2}(a_I - 1) \qquad E_m = \frac{1}{3}(E_1 + E_2 + E_3)$$

$$E_I' = E_I - E_m \qquad E_e = \sqrt{\frac{2}{3}\left(E_1'^2 + E_2'^2 + E_3'^2\right)}$$

V. Search the phase space $([E_e], [S_e])$ of one-dimensional data to obtain

$$\gamma = \frac{2}{3}\frac{S_e}{E_e}\bigg|_{X_g}$$

VI. Search the phase space $([E_J], [S_m])$ or $([E_m], [S_m])$ of one-dimensional data to obtain S_m

VII. Compute the stress S_{ij}

$$S_{ij}\big|_{X_g} = \sum_{I=1}^{3} \gamma E_I' (v_I)_i (v_I)_j + S_m \delta_{ij}$$

Box I. Algorithm for stress updates in MAP123.

5. Numerical examples

5.1. Driven by 1D data of numerical experiments

A $1 \times 1 \times 0.1$ plate with a circular hole of radius 0.1 at the center under the tensile loading is investigated first. The geometric setup and boundary conditions are shown in Fig. 6a. The displacement U is applied on the right surface and the maximum displacement is 1 (corresponding engineering strain 100%). The left surface is fixed in the x direction and the bottom surface is fixed in y direction. The front and back surfaces are fixed in the z direction. The boundary value problem is solved with the reference Odgen model and the proposed MAP123 method with the data-set of M_A. Note that the data-set of M_A in the proposed MAP123 method is generated by the reference Odgen model with the same material parameters. Fig. 6b shows the results of stress vs. engineering strain for both models. Both Cauchy stress F_R/A and nominal stress (defined as F_R/A_0) are shown, where F_R is the reaction force on the right edge with the imposed displacement. The engineering strain is defined as U/L. A very good agreement between the predictions by both models is observed. For the proposed MAP123 method, when the

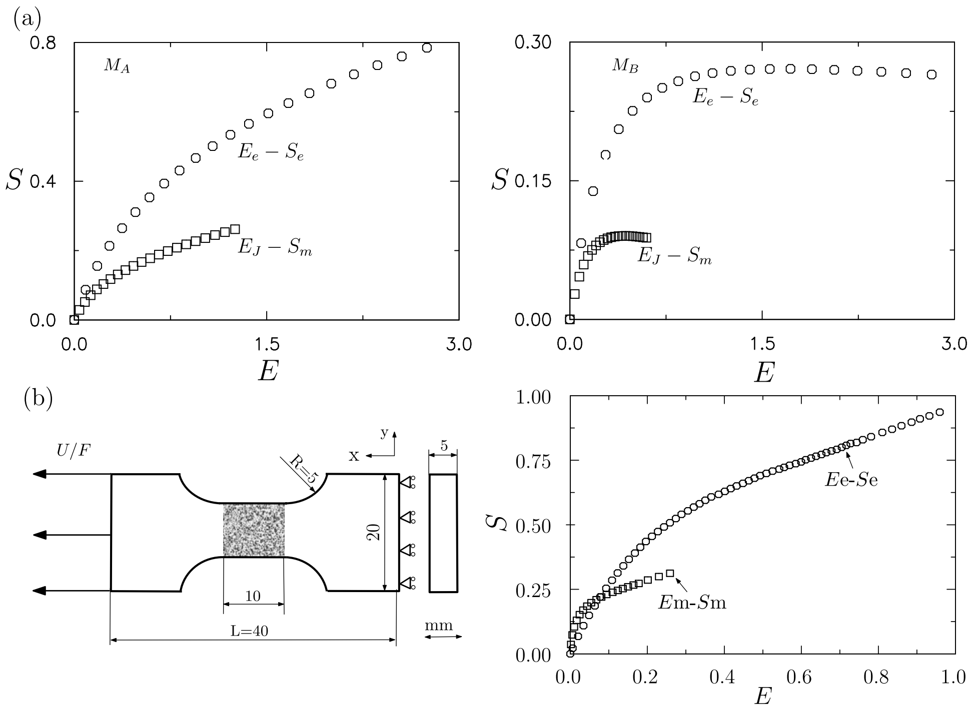

Fig. 5. (a) Two generated sets of one-dimension data ($[E_e]$, $[S_e]$) and ($[E_J]$, $[S_m]$) by numerical experiments of uniaxial tension with Odgen model, called M_A (left) and M_B (right). (b) The dimension of the specimen for 1D data generation in the physical experiments on the left. On the right, one-dimension data ($[E_e]$, $[S_e]$) and ($[E_m]$, $[S_m]$) generated by physical experiments of uniaxial tension, which are employed to solve boundary-value problems with void, ref. Fig. 17.

engineering strain is beyond 60%, the required stress–strain values for some material points are out of the range in the one-dimensional data. Thus the computation is terminated.

To test how the data-set can influence the simulation results, we run the simulations with 200, 500 and 1000 points of data-set by proposed MAP123 method. The same way is used to generate these data. The computational times to finish the simulations are 924, 1102 and 1279 seconds of wallclock time. The reference model takes 54 s of wallclock time. The data-driven approach is much slower than the reference model because the derivatives for the tangent stiffness take more time based on the pure data. The obtained results with different points of data-set are the same. Results are not shown here to save space.

Fig. 7 presents the contour of effective Cauchy stress predicted by the reference Odgen model and the proposed MAP123 method under three levels of imposed engineering strains ($U/L = 0.37$, 0.57 and 0.62). It is difficult to distinguish the difference obtained by these two models in the given strain ranges. The averaged relative error in terms of effective Cauchy stress is less than 0.5%. It confirms that the MAP123 method can effectively replace the traditional constitutive model to drive the 3D FEA on boundary-value problems of hyperelastic materials.

We are curious whether the choice of the boundary condition leads to the different performance of the proposed MAP123 method. Thus, we consider the same problem shown in Fig. 6 with different boundary conditions. The new boundary conditions are presented in Fig. 8a: the degrees of freedom in both x and y directions on the left surface are fixed; the bottom surface is traction free; the displacement U is still applied on the right surface and the maximum displacement is 2 (corresponding engineering strain 200%). Both the reference Odgen model and the proposed MAP123 method are considered. Fig. 8b shows the stress vs. engineering strain curves for both models. Both Cauchy stress F_R/A and nominal stress (defined as F_R/A_0) are shown, where F_R is the reaction force on the right edge with imposed displacement. The engineering strain is defined as U/L. A very good agreement between the reference and MAP123 models is observed when the engineering strain is less than 100%. When the imposed engineering strain is beyond 100%, the discrepancy between two models increases. The relative error in terms of nominal stress is smaller than that of Cauchy stress. Even under the imposed engineering strain 200%, the relative error in terms of Cauchy stress is around 6%.

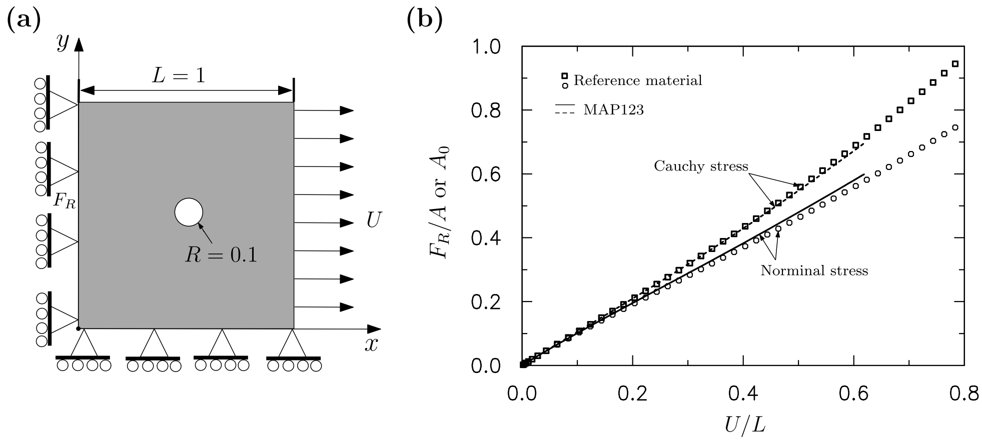

Fig. 6. Finite element analysis on a rectangular plate with a circular hole. (a) The geometric model and boundary conditions of the plate. The x direction of left edge and y direction of the bottom edge are fixed. (b) The stress–strain curves for the plate, predicted by the reference Odgen material law and the proposed data-driven MAP123 approach. The averaged Cauchy stress and nominal stress are defined as F_R/A and F_R/A_0 respectively, where F_R is the reaction force on the surface with the imposed displacement. A_0 is the surface area in the original configuration and A is in the current configuration. The average engineering strain is defined as U/L.

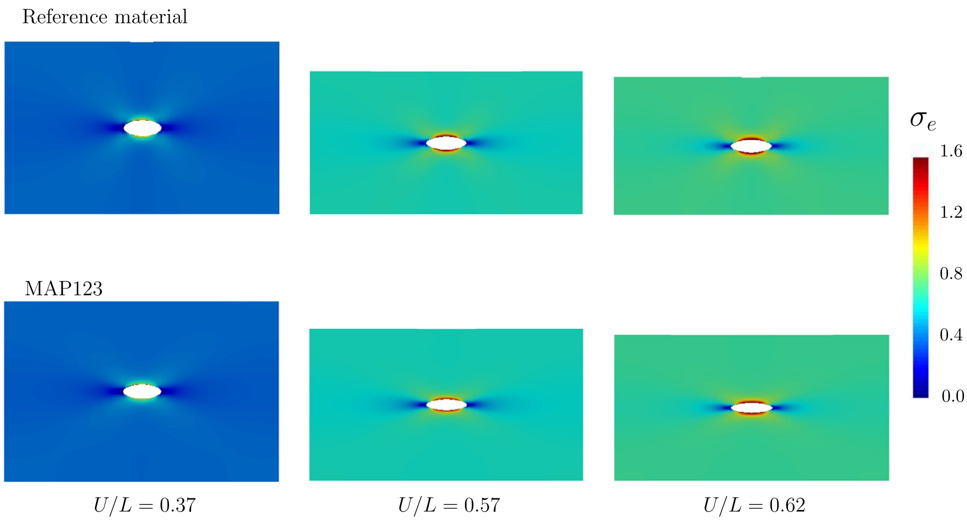

Fig. 7. Contour plots of effective Cauchy stress predicted by the reference Odgen material model and the proposed MAP123 method for the boundary value problem shown in Fig. 6 under the three different levels of imposed strain $U/L = 0.37$, 0.57 and 0.62.

Fig. 9 plots the contour of effective Cauchy stress predicted by the reference Odgen model and the proposed MAP123 method under three levels of imposed engineering strain ($U/L = 0.71$, 1.22 and 2.0). When the imposed engineering strain $U/L = 0.71$, a very good agreement between these two models for effective Cauchy stress is observed. When the imposed engineering strain $U/L = 1.22$, the predictions by both models for effective Cauchy stress are approximately the same. When the imposed engineering strain is very large and $U/L = 2.0$, the predictions by both models have somewhat discrepancies. The predicted stress contour by the MAP123 is more dispersed around the void while more localized by the reference Odgen model. The local difference of stress distribution leads to the discrepancy of the average stress shown in Fig. 8 at large deformation.

The data-driven approach such as the present one may not satisfy the assumption of material frame indifference for material laws. We run the simulations again from a different frame for the problem shown in Fig. 8a. The simulation domain is rotated 45° but the coordinate system and the boundary conditions are the same as that shown in Fig. 8a. The average nominal stress vs. the engineering strain for both models are plotted in Fig. 10b. Both

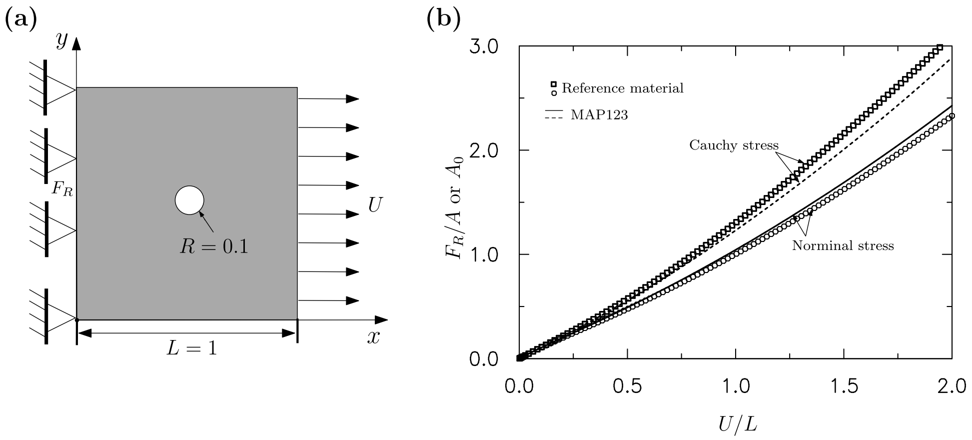

Fig. 8. Finite element analysis on a rectangular plate with a circular hole. (a) The geometric model and boundary conditions of the plate. Both the x and y degrees of freedom of the left edge are fixed. The displacement U is imposed on the right edge. (b) The stress–strain curves for the plate, predicted by the reference material model and the proposed MAP123 approach. The definitions of the average Cauchy stress, nominal stress, and the engineering strain are the same as those shown in Fig. 6.

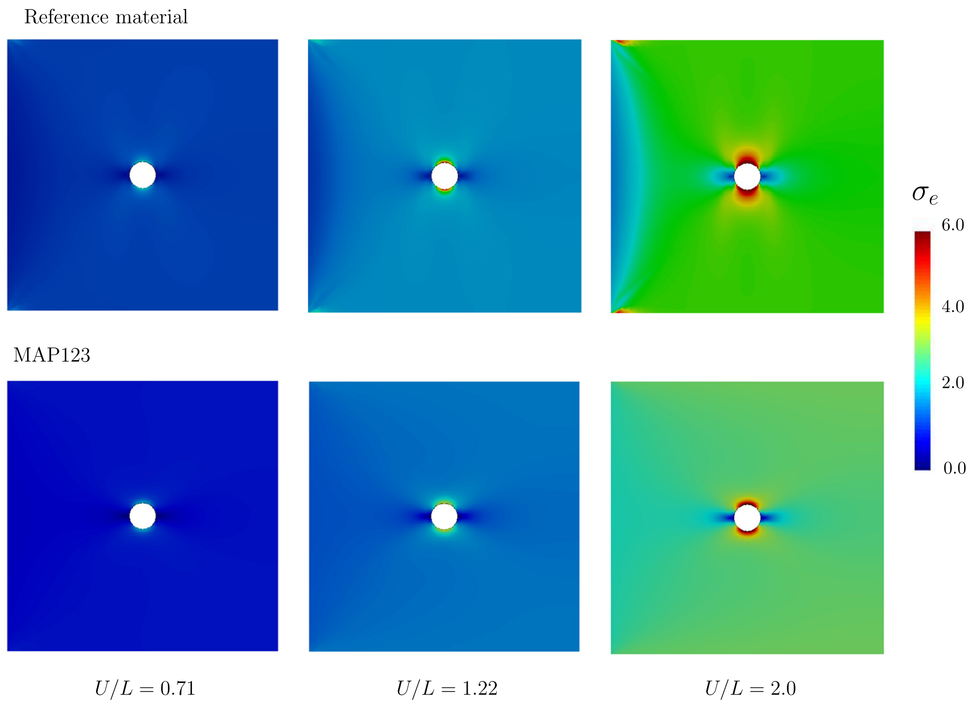

Fig. 9. Contour plots of effective Cauchy stress predicted by the reference Odgen model and the proposed MAP123 method for the model shown in Fig. 8 under three levels of imposed strain $U/L = 0.71$, 1.22 and 2.0.

models give the same stress vs. strain response. This confirms the assumption of material frame indifference for material laws. This can also be observed from Appendix B theoretically.

Previous examples only discuss the uniaxial loading on the simulation domain. It is close to the stress-state to generate the data-set. We then consider a different loading condition, under which the x and y degrees of freedom of the left edge and bottom edge are fixed respectively, and the front and back surfaces are traction free in the z direction. The displacements U and V are imposed on the right and top edges respectively, shown in Fig. 11. Both the reference Odgen model and the proposed MAP123 method are considered. Fig. 11b shows the stress vs.

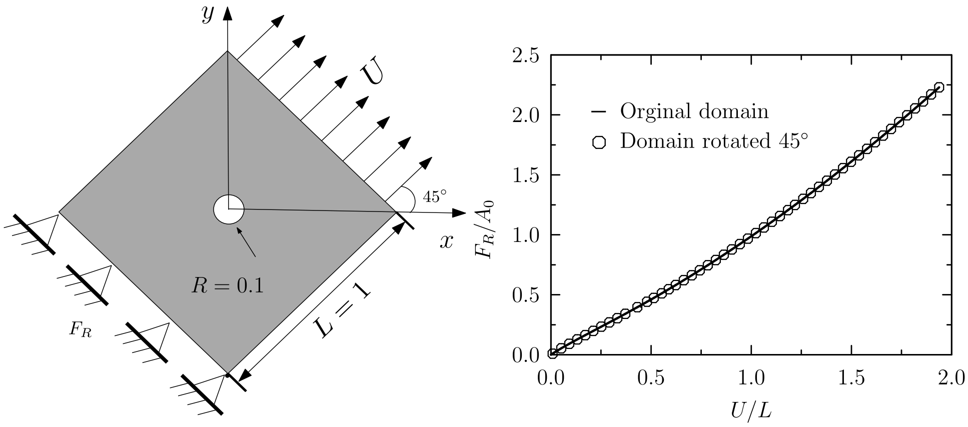

Fig. 10. Finite element analysis on a rotated plate with a circular hole under biaxial tension. The original coordinate system is the same as that shown in Fig. 8. (a) Except the geometric model is rotated 45°, boundary conditions are the same as that shown in Fig. 8. (b) The stress–strain curves predicted by the proposed MAP123 approach for unrotated geometric model and the rotated one. The definitions of the average nominal stress and the engineering strain are the same as those shown in Fig. 6.

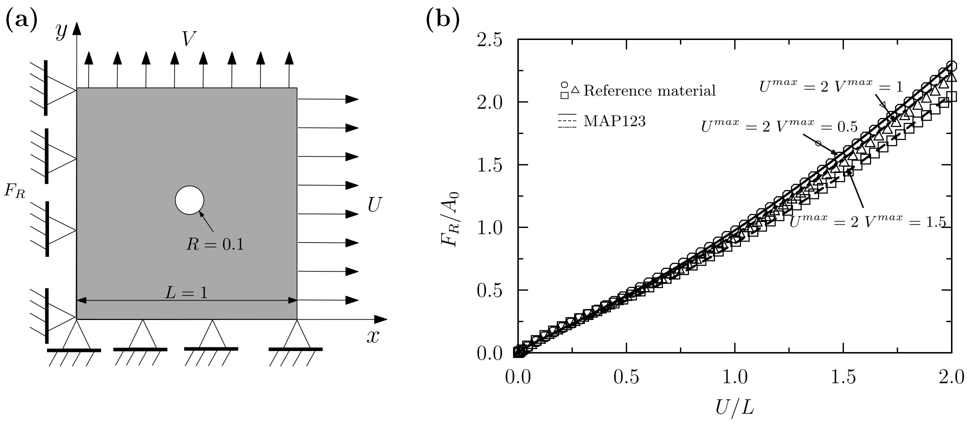

Fig. 11. Finite element analysis on a rectangular plate with a circular hole under biaxial tension. (a) The geometric model and boundary conditions of the plate. Both the x and y degrees of freedom of the left edge are fixed. The displacement U and V are imposed on the right and top edges respectively. (b) The stress–strain curves for the plate, predicted by the reference material model and the proposed MAP123 approach. The definitions of the average nominal stress and the engineering strain are the same as those shown in Fig. 6.

engineering strain curves for both models. The average nominal stress (defined as F_R/A_0) are shown, where F_R is the reaction force along the x direction on the right edge with imposed displacement. The engineering strain is defined as U/L. A very good agreement between the reference and MAP123 models is observed when the engineering strain is even around 200%.

Fig. 12 plots the contour of effective Cauchy stress in the current configuration under three levels of the imposed engineering strain $U/L = 0.6$, 1.0 and 2.0. For the comparison purpose, the results under the same level of the imposed engineering strain from the reference Odgen model are also shown. The predicted stress contour by the MAP123 is more dispersed around the void while more localized by the reference Odgen model at the large deformation. However, the general deformation patterns are very close to each other.

In previous examples, only one void in the simulation domain is considered. We are curious if the introduction of more voids can result in a different performance. We then study an example similar to that shown in Fig. 11a but eight voids are randomly distributed in the domain. The boundary conditions are: x and y degrees of freedom of the left edge and bottom edge are fixed respectively, and the front and back surfaces are traction free in the z direction. The displacements U and V are imposed on the right and top edges respectively, shown in Fig. 13a. The reference Odgen model and the proposed MAP123 method are considered. Fig. 13b shows the stress vs. engineering

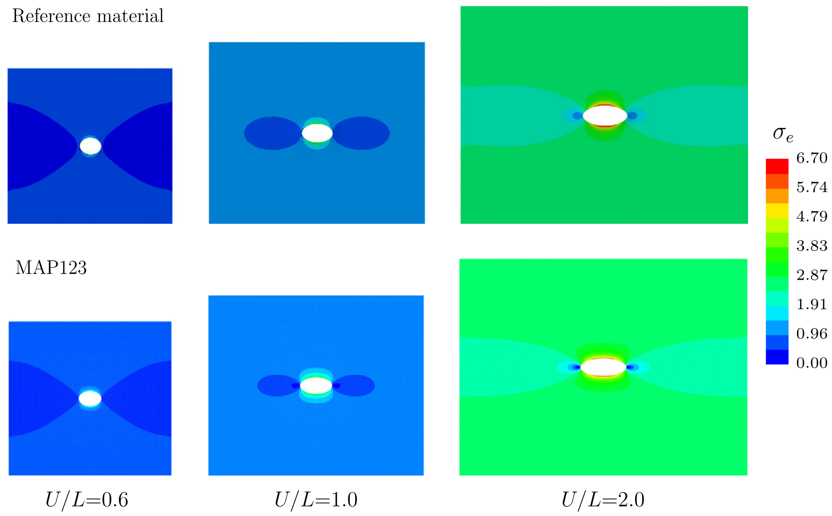

Fig. 12. Contour plots of effective Cauchy stress predicted by the reference Odgen model and the proposed MAP123 method for the model shown in Fig. 11 for the maximum displacements $U^{max} = 2$ and $V^{max} = 1$ under three levels of imposed strain $U/L = 0.6$, 1 and 2.

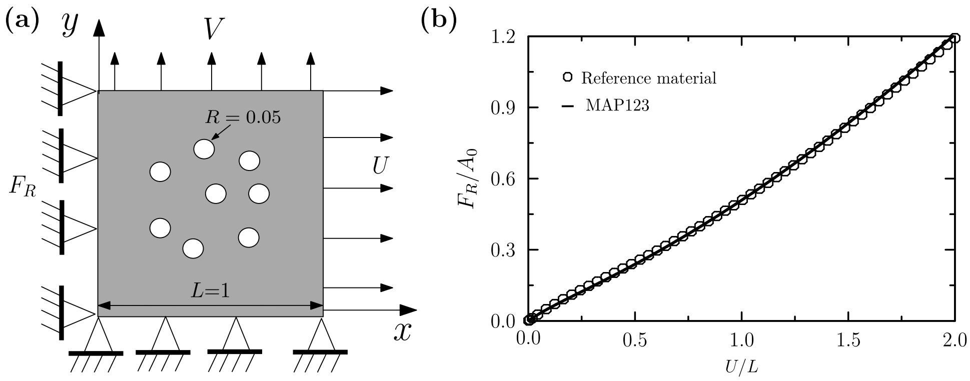

Fig. 13. Finite element analysis on a rectangular plate with multiple voids under biaxial tension. (a) The geometric model and boundary conditions of the plate. Both the x and y degrees of freedom of the left edge are fixed. The displacement U and V are imposed on the right and top edges respectively. The maximum displacements are $U^{max} = 2$ and $V^{max} = 1$. (b) The stress–strain curves for the plate, predicted by the reference material model and the proposed MAP123 approach. The definitions of the average nominal stress and the engineering strain are the same as those shown in Fig. 6.

strain curves for both models. The average nominal stress and the engineering strain are defined as before. It is still observed that the predictions by the reference model and MAP123 are almost the same when the engineering strain is even around 200%.

Fig. 14 plots the contour of effective Cauchy stress in the current configuration under three levels of the imposed engineering strain $U/L = 0.6$, 1.0 and 2.0. For the comparison purpose, the results under the same level of the imposed engineering strain from the reference Odgen model are also shown. The predicted stress contour by the MAP123 is almost the same as that by the reference model.

We finally consider a more complicated example. A $1 \times 1 \times 0.1$ matrix material with a circular particle/inclusion of radius 0.1 at the center under the tensile loading is investigated. The geometric setup and boundary conditions are shown in Fig. 15a. The displacement U is applied on the right surface and the maximum displacement is 0.5. The left surface is fixed in the x direction and the bottom surface is fixed in y direction. The front and back surfaces are fixed in the z direction. The boundary value problem is solved with the reference Odgen model and the proposed MAP123 model with the data-sets of M_A and M_B for matrix and particle, respectively. Fig. 15b shows the results of stress vs. engineering strain for both models. Both Cauchy stress F_R/A and nominal stress (defined as F_R/A_0)

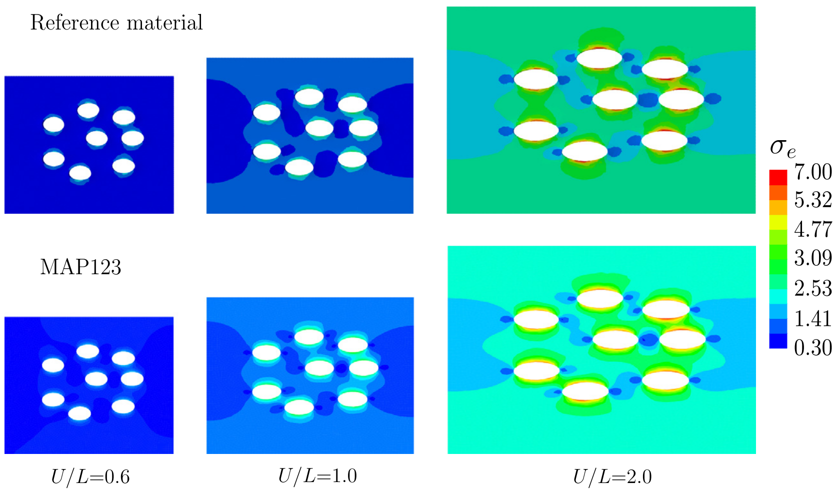

Fig. 14. Contour plots of effective Cauchy stress predicted by the reference Odgen model and the proposed MAP123 method for the model shown in Fig. 13 for the maximum displacements $U^{max} = 2$ and $V^{max} = 1$ under three levels of imposed strain $U/L = 0.6$, 1 and 2.

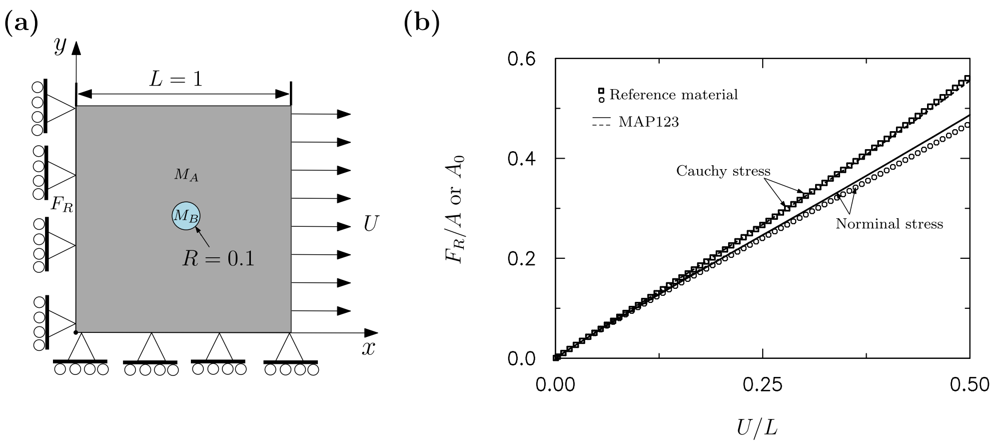

Fig. 15. Finite element analysis on a rectangular plate with a circular particle/inclusion. (a) The geometric model and boundary conditions of the plate. The left surface is fixed in the x direction and the bottom surface is fixed in y direction. The front and back surfaces are free in the z direction. The displacement U is imposed on the right edge. (b) The stress–strain curves for the plate, predicted by the reference material model and the proposed MAP123 approach. The definitions of the average Cauchy stress, nominal stress, and the engineering strain are the same as those shown in Fig. 6.

are shown, where F_R is the reaction force on the right edge with the imposed displacement. The engineering strain is defined as U/L. A very good agreement between the predictions by both models is observed.

Fig. 16 plots the contour of effective Cauchy stress in the current configuration under three levels of the imposed engineering strain $U/L = 0.16$, 0.35 and 0.5. For the comparison purpose, the results under the same level of the imposed engineering strain from the reference Odgen model are also shown. The outline of particle during the deformation is illustrated by the purple dashed-lines. It can be observed that the shape of particle and stress contour predicted by both models show good agreement. It further confirms the effectiveness and accuracy of the proposed MAP123 method.

5.2. Driven by 1D data of physical experiments

To verify the proposed MAP123 method, it is better to use the experimental data shown in Fig. 1 to address the MAP123 method because those are motivating examples where the traditionally used hyperelastic models fail.

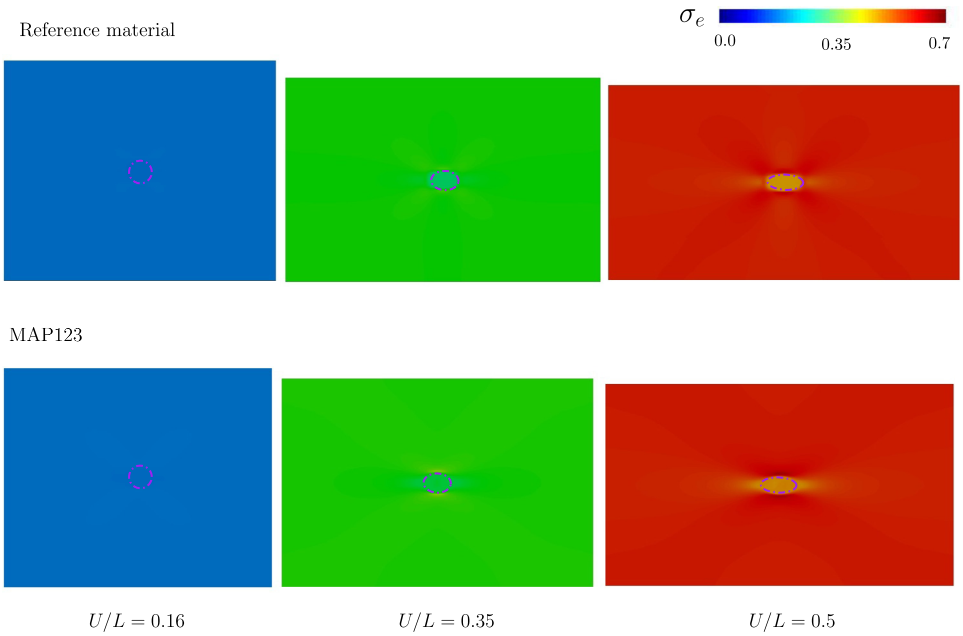

Fig. 16. Contour plots of effective Cauchy stress predicted by the reference Odgen model and the proposed MAP123 method for the model shown in Fig. 15 under three levels of imposed strain $U/L = 0.16$, 0.35 and 0.5.

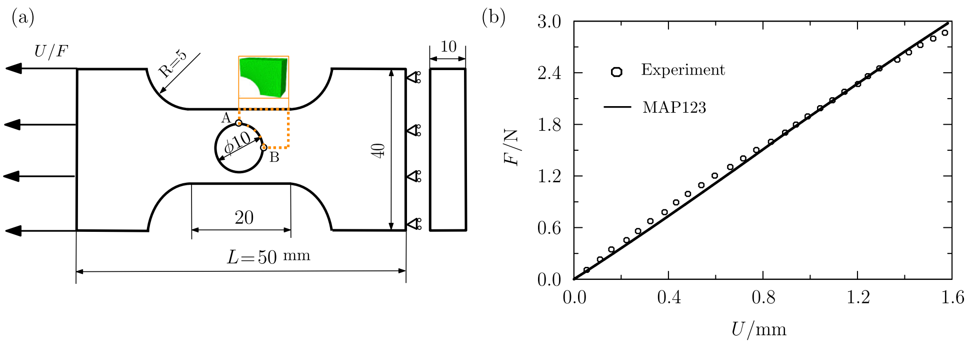

Fig. 17. (a) Physical experimental specimen with a void at the center under tensile loading at one end of it. The dimension of the specimen is also marked. The displacement U on the left side is imposed and the reaction force on right side is F. This boundary-value problem is solved by the data-set generated by the uniaxial tension of standard homogeneous specimen, shown in Fig. 5. (b) The reaction force vs. the imposed displacement predicted by the proposed MAP123 method and experiments.

However, we only record the uniaxial force and extension along the loading direction without three dimensional deformation recorded by DIC facility. Then it cannot be used to verify MAP123 method. Another thing is that the provider for the original materials does not produce them anymore. We fabricate a voided specimen with the same silicone rubber for generating the 1D data. The original materials for this silicone rubber are bought from Smooth-on company, USA. The specimen has a void with diameter 10 mm at the center, which is shown in Fig. 17a. The dimension of the specimen is also marked in the figure. Then the uniaxial tensile experiment is carried out on the specimen by a universal testing machine SHIMADZU EZ–LX. Digital Images Correlation (DIC) testing facility is also used to record the deformation of the specimen at each loading step around the area with void.

A finite element model is then built to simulate the deformation of specimen under tensile loading, which is shown in the inset of Fig. 17a. Due to the symmetry of the specimen, only one eighth of the specimen is used to build the model. The x, y and z symmetric boundary conditions are imposed on the left surface, back surface and the bottom surface. The displacement loading is imposed on the right surface, which is the same as that measured

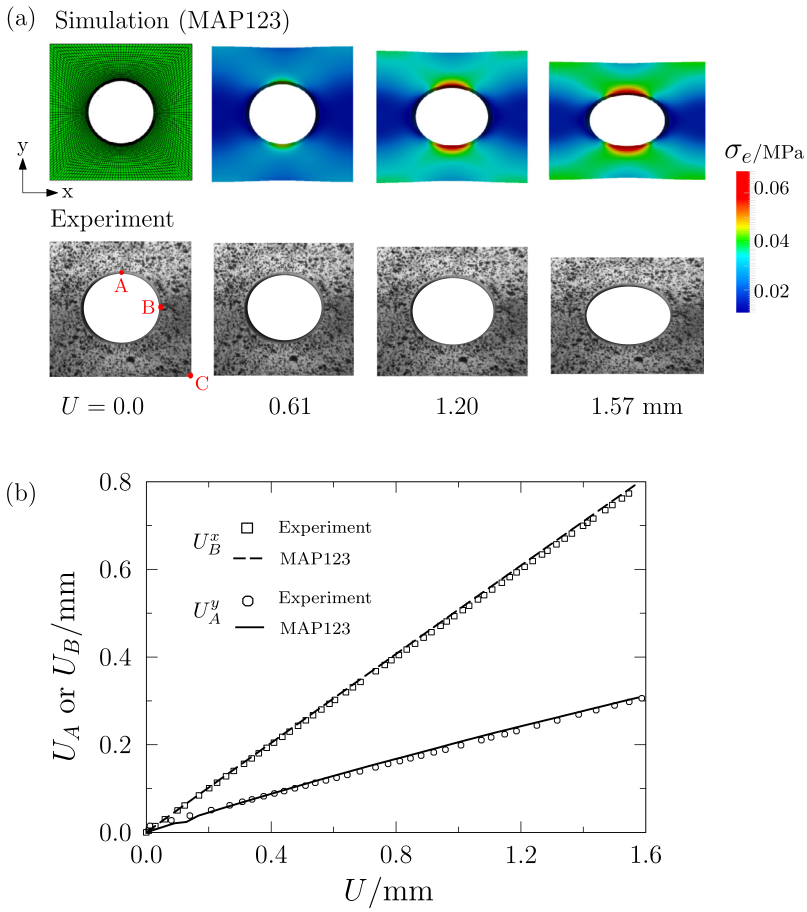

Fig. 18. (a) Deformation configurations of the specimen under the different levels of the imposed displacement $U = 0$, 0.61, 1.2 and 1.57 mm given by the proposed MAP123 and experiments. (b) Comparison of displacement of point A in y direction and point B in x direction between MAP123 predictions and experiment measurements. Points A and B are marked in Fig. 18a.

in the experiments. We then employ the MAP123 with the 1D data shown in Fig. 5 to solve this boundary-value problem. Fig. 17b plots the reaction force vs. the displacement for both simulation and experiments. It looks the MAP123 gives the almost the same response as the experiments. The deformation of specimen in the simulation is also compared with the experiments under the same level of displacement (see Fig. 18a). The shape of void under the same displacement is almost the same. The displacement in the y direction on the point of A and the displacement in the x direction on the point of B are further plotted as a function of imposed displacement, shown in Fig. 18b. The simulated displacement agrees well with the experiments. These results further prove the effectiveness and accuracy of the proposed MAP123.

6. Conclusion

To solve the 3D boundary-value problems in engineering applications, the 1D experimental data for material behaviors should be decompressed into 3D. We have proposed a method called MAP123 to decompress the 1D data for driving the 3D computation. The proposed MAP123 method is employed to solve several classical 3D boundary-value problems. Comparing to the same boundary-value problems with the reference material model, the solutions given by the proposed MAP123 method can approximate the reference ones very well. We also perform the physical experiments to generate the data. The generated data is used to solve a boundary-value problem for a specimen with one void at the center or multiple voids. The force/deformation versus displacement loading results are also compared with experiments and agree with experiments very well.

The proposed model-free approach is without the analytic function of material laws. Whatever the isotropic nonlinear elastic material is, only one parameter γ involved should be given by the data-set because the decomposition of stress and strain into deviatoric and spherical parts is applied to the isotropic nonlinear elastic materials at finite deformation. To build material model for nonlinear elastic solids until now, analytic mathematical function of energy density must be proposed first. Then the stress–strain relationship is derived through the analytic function. However, the proposed approach does not use any analytic mathematical function but the measured data of equivalent stress vs. equivalent strain, mean stress vs. mean strain. Based on the proposed approach, uniaxial experiment is suggested to measure the deformation in three directions not only along the uniaxial loading direction. This approach ignores the inner mechanism like many data-driven approaches, lessens the difficulty to choose the existing nonlinear elastic models and calibrate the parameters (often more than 2) involved in these models. These existing material models also may not be good enough for many new emerging materials because these existing models only can consider the well-known mechanisms of existing materials.

The present approach is limited to isotropic nonlinear elastic materials. It cannot be applied to path and history dependent materials such as elastoplastic materials directly. The third invariant of Green strain also should not vary too much during the deformation. If this condition cannot be satisfied, the proposed approach cannot work because the one-dimensional data cannot cover some special cases. This means under some specific loading conditions such as triaxial tension, the present approach can be used when the deformation is not too large but not at a relatively large deformation because the third invariant of Green strain will become large with the increased triaxial tension. To cover these loading conditions, a different way to design the use of the data should be proposed. This can be a future research direction.

Acknowledgments

S.T. appreciates the support from NSF of China (Project No. 11872139). X.G. Thanks the support from NSF of China (11732004, 11821202), and Program for Changjiang Scholars, China, Innovative Research Team in University (PCSIRT). WKL acknowledged the support of the US National Science Foundation (NSF) under Grant No. MOMS/CMMI-1762035.

Appendix A. Theory of MAP123 for data expansion from 1D to 3D

The theory of MAP123 is explained in this section. Notations and key concepts of continuum mechanics are employed [4]. A material particle $\mathbf{X}$ in the body Ω moves to the current position $\mathbf{x}$ by a displacement $\mathbf{u}$:

$$\mathbf{x} = \mathbf{X} + \mathbf{u}(\mathbf{X}), \qquad \mathbf{X} \in \Omega. \tag{4}$$

The deformation gradient at the material point $\mathbf{X}$ is defined as

$$\mathbf{F} = \partial\mathbf{x}/\partial\mathbf{X} \tag{5}$$

with Jacobian $J = \det(\mathbf{F})$. The right Cauchy–Green tensor $\mathbf{C}$ is defined:

$$\mathbf{C} = \mathbf{F}^T\mathbf{F} \tag{6}$$

which is symmetric and can be expressed in the principal space:

$$\mathbf{C} = a_i \mathbf{N}_i \otimes \mathbf{N}_i \tag{7}$$

Here a_i $(i = 1 \cdots 3)$ are the principal values of $\mathbf{C}$ and $\mathbf{N}_i$ $(i = 1 \cdots 3)$ are the principal vectors. For the material belongs to the family of isotropic nonlinear elastic solids, the secondary PK stress can be expressed in the similar way:

$$\mathbf{S} = S_i \mathbf{N}_i \otimes \mathbf{N}_i \tag{8}$$

where S_i $(i = 1 \cdots 3)$ are the principal values and the principal eigenvectors are the same as those of $\mathbf{C}$. This coaxial relation between the secondary PK stress and right Cauchy–Green tensor is very convenient for us to generalize the data directly from 1D to 3D.

The Green strain is defined as:

$$\mathbf{E} = \frac{1}{2}(\mathbf{C} - \mathbf{I}) \tag{9}$$

which can also be expressed in the principal space as:

$$\mathbf{E} = E_i \mathbf{N}_i \otimes \mathbf{N}_i \tag{10}$$

with $E_i = \frac{1}{2}(a_i - 1)$. We define the effective strain:

$$E_e = \sqrt{\frac{2}{3}\left(E_1'^2 + E_2'^2 + E_3'^2\right)} \tag{11}$$

$$E_i' = E_i - E_m$$

with $E_m = (E_1 + E_2 + E_3)/3$. The effective stress is similarly defined:

$$S_e = \sqrt{\frac{3}{2}\left(S_1'^2 + S_2'^2 + S_3'^2\right)} \tag{12}$$

where

$$S_i' = S_i - S_m \tag{13}$$

with $S_m = \frac{1}{3}(S_1 + S_2 + S_3)$.

The stress can be decomposed into hydrostatic and deviatoric parts:

$$S_{ij} = \sum_{I=1}^{3} S_I' (N_I)_i (N_I)_j + S_m \delta_{ij} \tag{14}$$

To unzip the data from 1D to 3D, the fact that the deviatoric stress is coaxial with deviatoric strain is employed:

$$\frac{S_1'}{E_1'} = \frac{S_2'}{E_2'} = \frac{S_3'}{E_3'} = \gamma \tag{15}$$

It is discussed in Appendix B. With this fact at hand, the effective stress can be expressed as

$$S_e = \gamma \sqrt{\frac{3}{2}\left(E_1'^2 + E_2'^2 + E_3'^2\right)} = \frac{3}{2} E_e \gamma \tag{16}$$

Through the experiments under uniaxial tension or compression, the data for effective stress vs. effective strain can be obtained:

$$E_e \Leftrightarrow S_e \tag{17}$$

A data searching strategy for the corresponding (E_e, S_e) in the phase space has to be proposed, which can be referred to the available algorithms in computational graphics [37]. Then γ can be solved easily

$$\gamma = \frac{2}{3}\frac{S_e}{E_e} \tag{18}$$

based on the experimentally obtained data of $([E_e], [S_e])$. Through the uniaxial compression or tension experiments, the volume change of material ($E_J = J - 1$ or E_m) and hydrostatic stress can also be measured. The measured experimental data of $([E_J], [S_m])$ also can be expressed in phase space:

$$E_J \Leftrightarrow S_m \tag{19}$$

The similar data searching strategy can be applied to obtain the corresponding $([E_J], [S_m])$ or $([E_m], [S_m])$.

Through the above proposed method, it is possible to express the measured experimental data in phase space $([E_e], [S_e])$ and $([E_J], [S_m])$ into three dimensional forms S_{ij}, which can be used to describe the stress–strain response of the material.

Appendix B. Coaxial relationship between deviatoric stress and strain

In this appendix, we will show Eq. (15) can be satisfied. For isotropic hyperelastic material, the second PK stress can be derived through the energy function $\Psi(I_E, II_E, III_E)$ per unit mass where I_E, II_E, III_E are invariants of

Green strain $\mathbf{E}$. If we make an assumption that the third invariant of strain is not considered. Then the energy function takes $\Psi(I_E, II_E)$. The second PK stress can be obtained

$$\begin{aligned}\mathbf{S} &= \frac{\partial \Psi(I_E, II_E)}{\partial \mathbf{E}} \\ &= \frac{\partial \Psi}{\partial I_E}\mathbf{1}+\frac{\partial \Psi}{\partial II_E}\left(I_E\mathbf{1}-\mathbf{E}\right)\end{aligned} \tag{20}$$

where $\mathbf{1}$ is identity tensor. Substituting the strain decomposition

$$\mathbf{E} = \mathbf{E}^{'} + E_m\mathbf{1}$$

into Eq. (20), then

$$\begin{aligned}\mathbf{S} &= \frac{\partial \Psi}{\partial I_E}\mathbf{1}+\frac{\partial \Psi}{\partial II_E}\left(I_E\mathbf{1}-\mathbf{E}^{'}-E_m\mathbf{1}\right) \\ &= \left(\frac{\partial \Psi}{\partial I_E}+\frac{\partial \Psi}{\partial II_E}2E_m\right)\mathbf{1}-\frac{\partial \Psi}{\partial II_E}\mathbf{E}^{'}\end{aligned}$$

where $I_E = \mathrm{tr}(\mathbf{E}) = 3E_m$ is used.

$$\begin{aligned}S_m &= \frac{\partial \Psi}{\partial I_E}+\frac{\partial \Psi}{\partial II_E}2E_m \\ \mathbf{S}^{'} &= -\frac{\partial \Psi}{\partial II_E}\mathbf{E}^{'}\end{aligned}$$

With the decomposition of deviatoric strain and stress

$$\mathbf{E}^{'} = \sum_{I=1}^{3} E_I^{\prime}\mathbf{N}_I \otimes \mathbf{N}_I \qquad \mathbf{S}^{'} = \sum_{I=1}^{3} S_I^{\prime}\mathbf{N}_I \otimes \mathbf{N}_I$$

It leads to

$$S_I^{'} = -\frac{\partial \Psi}{\partial II_E}E_I^{\prime}$$

Then γ involved in Eq. (15) in the context and Appendix A is

$$\gamma = -\frac{\partial \Psi}{\partial II_E}$$

which is a function of I_E and II_E and can be determined by the measured data. The advantage of model-free data-driven approach can avoid the construction of energy function and its derivatives. If the energy function involves the third invariant III_E, the Second PK stress can be derived as

$$\begin{aligned}\mathbf{S} &= \frac{\partial \Psi}{\partial \mathbf{E}} \\ &= \frac{\partial \Psi}{\partial I_E}\mathbf{1}+\frac{\partial \Psi}{\partial II_E}\left(I_E\mathbf{1}-\mathbf{E}\right)+\frac{\partial \Psi}{\partial III_E}III_E\mathbf{E}^{-1} \\ &= \frac{\partial \Psi}{\partial I_E}\mathbf{1}+\frac{\partial \Psi}{\partial II_E}\left(I_E\mathbf{1}-\mathbf{E}\right)+\frac{\partial \Psi}{\partial III_E}III_E\mathbf{E}^{-1} \\ &= \frac{\partial \Psi}{\partial I_E}\mathbf{1}+\frac{\partial \Psi}{\partial II_E}\left(I_E\mathbf{1}-\mathbf{E}\right)+\frac{\partial \Psi}{\partial III_E}III_E\left(\mathbf{E}^{'}+E_m\mathbf{1}\right)^{-1}\end{aligned}$$

in which

$$\left(\mathbf{E}^{'}+E_m\mathbf{1}\right)^{-1} = a\mathbf{E}^{\prime 2}+b\mathbf{E}^{\prime}+c\mathbf{1}$$

where

$$a = \frac{1}{III_{E'}+E_m^3+II_{E'}E_m}, b = -\frac{E_m}{III_{E'}+E_m^3+II_{E'}E_m}, c = \frac{II_{E'}+E_m^2}{III_{E'}+E_m^3+II_{E'}E_m}$$

Here $II_{E'}$ and $III_{E'}$ are invariants of deviatoric strain $\mathbf{E}^{'}$ of Green strain $\mathbf{E}$. To get a, b, and c, Cayley–Hamilton theorem needs to be used, that is,

$$\boldsymbol{E}'^{3} - I_{E'}\boldsymbol{E}'^{2} + II_{E'}\boldsymbol{E}^{'} - III_{E'}\mathbf{1} = 0$$

Finally the second PK stress can be rewritten as

$$\begin{aligned}\mathbf{S} &= \frac{\partial\Psi}{\partial I_E}\mathbf{1}+\frac{\partial\Psi}{\partial II_E}\left(I_E\mathbf{1}-\mathbf{E}^{'}-E_m\mathbf{1}\right)+\frac{\partial\Psi}{\partial III_E}III_E\left(a\mathbf{E}'^{2}+b\mathbf{E}'+c\mathbf{1}\right)\\ &= \left(\frac{\partial\Psi}{\partial I_E}+2E_m\frac{\partial\Psi}{\partial II_E}+c\frac{\partial\Psi}{\partial III_E}III_E\right)\mathbf{1}+a\frac{\partial\Psi}{\partial III_E}III_E\mathbf{E}'^{2}+\left(\frac{\partial\Psi}{\partial III_E}III_E b-\frac{\partial\Psi}{\partial II_E}\right)\mathbf{E}^{'}\end{aligned}$$

Then the spherical part and the deviatoric part of the Second PK stress are

$$\begin{aligned}S_m &= \left(\frac{\partial\Psi}{\partial I_E}+2E_m\frac{\partial\Psi}{\partial II_E}+c\frac{\partial\Psi}{\partial III_E}III_E\right)+a\frac{\partial\Psi}{\partial III_E}III_E\ \mathrm{tr}\left(\mathbf{E}'^{2}\right)/3\\ \mathbf{S}^{'} &= a\frac{\partial\Psi}{\partial III_E}III_E\left(\mathbf{E}'^{2}-\mathrm{tr}\left(\mathbf{E}'^{2}\right)/3\mathbf{1}\right)+\left(\frac{\partial\Psi}{\partial III_E}III_E b-\frac{\partial\Psi}{\partial II_E}\right)\mathbf{E}^{'}\end{aligned}$$

From the above equation, $\mathbf{E}'^{2} \ll \mathbf{E}'$ when the deformation is not too large. Then if the energy function is weakly dependent on III_E, the coaxial relationship between deviatoric stress and strain still holds approximately. In general, if III_E varies too much during the deformation, Eq. (15) is not satisfied, which is the limitation of the proposed MAP123 approach. It is possible to overcome this issue by designing the use of data in a different way. Further works should be carried out.

References

[1] J.C. Simo, T.J. Hughes, Computational Inelasticity, Vol. 7, Springer Science & Business Media, 2006.
[2] J.E. Marsden, T.J. Hughes, Mathematical Foundations of Elasticity, Courier Corporation, 1994.
[3] T.J. Hughes, The Finite Element Method: Linear Static and Dynamic Finite Element Analysis, Courier Corporation, 2012.
[4] T. Belytschko, W.K. Liu, B. Moran, K. Elkhodary, Nonlinear Finite Elements for Continua and Structures, John wiley & sons, 2013.
[5] T. Kirchdoerfer, M. Ortiz, Data driven computational mechanics, Comput. Methods Appl. Mech. Engrg. 304 (2016) 81–101.
[6] T. Kirchdoerfer, M. Ortiz, Data-driven computing in dynamics, Internat. J. Numer. Methods Engrg. 113 (11) (2017) 1697–1710.
[7] T. Kirchdoerfer, M. Ortiz, Data driven computing with noisy material data sets, Comput. Methods Appl. Mech. Engrg. 326 (2017) 622–641.
[8] S. Conti, S. Müller, M. Ortiz, Data driven problems in elasticity, Arch. Ration. Mech. Anal. 229 (1) (2017) 79–123.
[9] A. Leygue, M. Coret, J. Rthor, L. Stainier, E. Verron, Data based derivation of material response, Comput. Methods Appl. Mech. Engrg. 331 (2018) 184–196.
[10] F. Chinesta, P. Ladeveze, R. Ibanez, J.V. Aguado, E. Abisset-Chavanne, E. Cueto, Data-driven computational plasticity, Procedia Eng. 207 (2017) 209–214.
[11] A.F. Bower, Applied Mechanics of Solids, CRC press, 2009.
[12] M. Mooney, A theory of large elastic deformation, J. Appl. Phys. 11 (9) (1940) 582–592.
[13] R.W. Ogden, Large deformation isotropic elasticity–on the correlation of theory and experiment for incompressible rubberlike solids, Proc. R. Soc. Lond. Ser. A Math. Phys. Eng. Sci. 326 (1567) (1972) 565–584.
[14] E.M. Arruda, M.C. Boyce, A 3-dimensional constitutive model for the large stretch behavior of rubber elastic materials, J. Mech. Phys. Solids 41 (2) (1993) 389–412.
[15] Z. Li, Z. Zhou, Y. Li, S. Tang, Effect of cyclic loading on surface instability of silicone rubber under compression, Polymers 9 (4) (2017) 148.
[16] Y. Li, S. Tang, B.C. Abberton, M. Kröger, C. Burkhart, B. Jiang, G.J. Papakonstantopoulos, M. Poldneff, W.K. Liu, A predictive multiscale computational framework for viscoelastic properties of linear polymers, Polymer 53 (25) (2012) 5935–5952.
[17] Y. Li, S. Tang, M. Kröger, W.K. Liu, Molecular simulation guided constitutive modeling on finite strain viscoelasticity of elastomers, J. Mech. Phys. Solids 88 (2016) 204–226.
[18] Z. Liu, J.A. Moore, W.K. Liu, An extended micromechanics method for probing interphase properties in polymer nanocomposites, J. Mech. Phys. Solids 95 (2016) 663–680.
[19] C. He, J. Ge, D. Qi, J. Gao, Y. Chen, J. Liang, D. Fang, A multiscale elasto-plastic damage model for the nonlinear behavior of 3d braided composites, Compos. Sci. Technol. 171 (2019) 21–33.
[20] Q. Wang, G.R. Gossweiler, S.L. Craig, X. Zhao, Mechanics of mechanochemically responsive elastomers, J. Mech. Phys. Solids 82 (2015) 320–344.
[21] Z. Liu, C. Wu, M. Koishi, A deep material network for multiscale topology learning and accelerated nonlinear modeling of heterogeneous materials, Comput. Methods Appl. Mech. Engrg. 345 (2019) 1138–1168.
[22] M.A. Bessa, R. Bostanabad, Z. Liu, A. Hu, D.W. Apley, C. Brinson, W. Chen, W.K. Liu, A framework for data-driven analysis of materials under uncertainty: countering the curse of dimensionality, Comput. Methods Appl. Mech. Engrg. 320 (2017) 633–667.

[23] A. Oishi, G. Yagawa, Computational mechanics enhanced by deep learning, Comput. Methods Appl. Mech. Engrg. 327 (2017) 327–351.
[24] M. Bessa, S. Pellegrino, Design of ultra-thin shell structures in the stochastic post-buckling range using bayesian machine learning and optimization, Int. J. Solids Struct. 139 (2018) 174–188.
[25] K. Wang, W. Sun, A multiscale multi-permeability poroplasticity model linked by recursive homogenizations and deep learning, Comput. Methods Appl. Mech. Engrg. 334 (2018) 337–380.
[26] K. Wang, W. Sun, Meta-modeling game for deriving theory-consistent, microstructure-based traction–separation laws via deep reinforcement learning, Comput. Methods Appl. Mech. Engrg. 346 (2019) 216–241.
[27] X. Lei, C. Liu, Z. Du, W. Zhang, X. Guo, Machine learning-driven real-time topology optimization under moving morphable component-based framework, J. Appl. Mech. 86 (1) (2019) 011004.
[28] I. Jolliffe, Principal component analysis, in: International Encyclopedia of Statistical Science, Springer, 2011, pp. 1094–1096.
[29] S. Wold, K. Esbensen, P. Geladi, Principal component analysis, Chemometr. Intell. Lab. Syst. 2 (1–3) (1987) 37–52.
[30] H. Abdi, L.J. Williams, Principal component analysis, Wiley Interdiscip. Rev. Comput. Stat. 2 (4) (2010) 433–459.
[31] C.M. Bishop, N.M. Nasrabadi, Pattern Recognition and Machine Learning, Academic Press, 2006.
[32] R. Hill, The Mathematical Theory of Plasticity, OXford University Press, 1998.
[33] R. Hill, J.R. Rice, Constitutive analysis of elastic-plastic crystals at arbitrary strain, J. Mech. Phys. Solids 20 (6) (1972) 401–413.
[34] S. Tang, T.F. Guo, L. Cheng, Rate effects on toughness in elastic nonlinear viscous solids, J. Mech. Phys. Solids 56 (3) (2008) 974–992.
[35] W.H. Wong, T.F. Guo, On the energetics of tensile and shear void coalescences, J. Mech. Phys. Solids 82 (2015) 259–286.
[36] Z.G. Liu, W.H. Wong, T.F. Guo, Void behaviors from low to high triaxialities: Transition from void collapse to void coalescence, Int. J. Plast. 84 (2016) 183–202.
[37] M.d. Berg, O. Cheong, M.v. Kreveld, M. Overmars, Computational Geometry: Algorithms and Applications, Springer-Verlag TELOS, 2008.